Catalysis Science & Technology

ROYAL SOCIETY OF CHEMISTRY

PAPER

View Article Online
View Journal | View Issue

Check for updates

Cite this: *Catal. Sci. Technol.*, 2026, **16**, 390

X-ray absorption and diffraction computed tomography characterization of deactivation and coking in spray-dried ZSM-5/alumina catalysts

Izar Capel Berdiell, *[a] Tomás Cordero-Lanzac,[a] Nicolai Haaber Junge,[a] Liebert Parreiras Nogueira, [b] Gavin Vaughan, [c] Marco Di Michiel,[c] Pablo Beato, [d] Lars F. Lundegaard,[d] David Wragg [ae] and Stian Svelle *[a]

One of the main drawbacks of acid-based heterogeneous catalytic processes involving hydrocarbons is coke formation. Still, research on shaped catalysts remains limited. The main objective of this study was to gain insight into the catalyst deactivation in the methanol-to-hydrocarbon (MTH) reaction. Diffraction and absorption computed tomography experiments were performed on spray dried, hollow semi-spherically shaped ZSM-5/alumina catalysts of approximately 250 microns in size. The catalysts were employed in the MTH reaction at two different pressures, resulting in varying degrees of coking. Absorption tomography (0.027 μm^3 per voxel) revealed the structural features and sponginess of the shaped catalysts. These are not perfect spheres; they rather have openings as they burst during the spray drying process. Further, high resolution powder X-ray diffraction computed tomography slices (0.125 μm^3 per voxel) were analyzed by parametric Rietveld refinement. The analysis showed that the catalyst and binder overall are rather homogeneously spatially distributed within each sphere, but bubbles and agglomerates of a single phase are frequent. In addition, it is demonstrated that there were no coking gradients across the sphere wall at both partial and full deactivation. This indicates that the binder and the catalyst shape and size were suitable for the reaction conditions. Indeed, the catalyst lifetime was almost doubled relative to the pure, powdered zeolite catalyst. A series of catalysts with varying degrees of deactivation have been fully characterized *ex situ*, suggesting significant spillover of coke from the zeolite to the alumina matrix. These findings demonstrate the need for greater efforts to understand the formulation of shaped catalyst objects, where the matrix should not only hold the components together but also support and enhance the overall catalytic process.

Received 22nd August 2025,
Accepted 20th November 2025

DOI: 10.1039/d5cy01023c

rsc.li/catalysis

Open Access Article. Published on 20 november 2025. Downloaded on 17.5.2026. 12.51.47.
This article is licensed under a Creative Commons Attribution 3.0 Unported Licence.

Introduction

Catalysts formulated into shaped objects have many practical advantages for industrial applications such as reduced pressure drop in reactor beds and increased thermal and mechanical resistance or heat conductivity. Common forms of shaping catalysts include high-pressure agglomeration (pellet formation), cohesive liquid agglomeration (granulation), or methods starting with slurries, which are either pushed to a profiled die and cut (extrusion) or atomized into a hot chamber (spray drying). However, research on such composite materials is rather scarce compared to pure polycrystalline catalysts because the multicomponent mixture adds variables that complicate the full understanding of the system.

Methanol to hydrocarbon conversion (MTH) is a well-known shape selective reaction that can be catalyzed by zeolites with several different pore sizes. Coke formation is a key cause of deactivation and therefore MTH has been used as a model reaction for investigations into coke formation. Different techniques have been proposed to extend the lifetime of zeolites during MTH, including controlling their acid site density, distribution or strength or tailoring their porosity.[1–3] Huge efforts have also been made to understand how coke species evolve during the reaction.[4–6] We have shown that X-ray diffraction (XRD) is a very reliable technique for tracking the evolution of zeolite deactivation during MTH. Operando XRD provides especially useful information by revealing the changes that occur in the zeolite structure during the reaction on ferrierite,[7] beta[8] and ZSM-5[9–11] and zeotype catalysts.[12] Some structural chemistry research has

[a] *Department of Chemistry, Center for Materials Science and Nanotechnology (SMN), University of Oslo, P.O. Box 1033 Blindern, N-0315 Oslo, Norway. E-mail: izarc@uio.no*
[b] *Oral Research Laboratory, Institute of Clinical Dentistry, Faculty of Dentistry, University of Oslo, P.O. Box 1033, Blindern, N-1143 Oslo, Norway*
[c] *ESRF-The European Synchrotron, 71 Avenue des Martyrs, 38000 Grenoble, France*
[d] *Topsoe A/S, Haldor Topsøes Allé 1, 2800 Kgs. Lyngby, Denmark*
[e] *IFE Institute for Energy Technology, Instituttveien 18, 2007 Kjeller, Norway*

This journal is © The Royal Society of Chemistry 2026

Open Access Article. Published on 20 novembar 2025. Downloaded on 17.5.2026. 12.51.47.
This article is licensed under a Creative Commons Attribution 3.0 Unported Licence.

been conducted with catalyst bodies of the type used in industrial reactors, in which the zeolite is agglomerated with different binders and inert fillers.[13–16] These demonstrated significant changes, not only in the catalyst lifetime, but also in the product distribution, thereby highlighting the need for more research on shaped catalysts.

Powder X-ray diffraction computed tomography (PXRD-CT) and total scattering computed tomography (PDF-CT) are 4-dimensional imaging techniques where the tomograms are a three-dimensional matrix of voxels in space with the fourth dimension comprising chemical information: every voxel of the PXRD-CT tomogram contains a powder XRD pattern, from which the crystal structure can be studied.[17,18] Our XRD-based techniques have previously been proven to be useful for exploring industrial-like zeolite extrudates as big as 1.8 ± 0.1 mm in diameter.[19,20] The main finding was the presence of radially distributed coking gradients due to diffusion limitations that led to heterogeneous catalyst deactivation. It was observed that almost one third of the extrudate remained untouched even after severe deactivation, and it seems likely that a large amount of the catalyst often may remain unused, making the materials less efficient as industrial catalysts.

In this work, we turned our attention to spray dried hollow spheres[21] and conducted deactivation studies of MTH in a range of pressures. Deactivation was first followed by different *ex situ* techniques, including our XRD analysis, to assess the levels of deactivation in the objects. We have also utilized computed tomography (CT) imaging based on absorption of X-rays to provide remarkable detail on the global and internal structure of the sphere. Moreover, we have employed PXRD-CT at, to the best of our knowledge, the highest resolution ever before on a catalyst composite. Although 4th generation synchrotrons and state-of-the-art optics are making the production of sub-micron X-ray beams routine, such beams accentuate the problems caused when the PXRD-CT beam is smaller than the crystallites and due to low flux in the voxels. Because of this, very few sub-micron PXRD-CT studies have been reported.[22] Our XRD descriptors for ZSM-5[19,20] have been assessed for huge PXRD-CT datasets, and we find an absence of coking gradients across the catalyst particles, suggesting that the spray dried spheres have a geometry that is optimized for effective utilization.

Experimental

Catalyst preparation

The ZSM-5 zeolite is commercially available from Zeolyst International (CBV 8014), with a Si/Al ratio of 40. The nominal composition of the slurry by dry weight was 40% CBV 8014 zeolite and 60% alumina precursor (Catapal B). The shaping of the catalyst was performed as described elsewhere.[21]

Catalyst testing

The catalysts were tested at both low- and high-pressure (Fig. 1). The catalytic reactions at atmospheric pressure were performed in a fixed-bed quartz reactor with the shaped catalyst objects fixed with glass wool. The inner diameter of the reactor was 6 mm. The reaction temperature was monitored using a thermocouple protected by a 3 mm wide quartz sleeve inserted into the middle of the catalyst layer. For each experimental run, the reactor was loaded with 125 mg of catalyst. Prior to the reaction, the catalyst was activated with an initial heating ramp of 10 °C min^{-1} under 20% O_2 in N_2 to 550 °C, and the temperature was kept for 1 h under O_2. Then, the catalytic bed was cooled to 400 °C reaction temperature under an Ar flow. Then, the MTH reaction was carried out at 307 mbar partial pressure of methanol (MeOH) balanced with He (purity 5.0). The total flow was 26 mL min^{-1} (8 mL min^{-1} MeOH and 18 mL min^{-1} He), giving a space velocity of 12.5 g_{MeOH} $g_{catalyst}^{-1}$ h^{-1}. The partial pressure of MeOH was controlled with a condenser set at 37 °C. The effluent from the reactor was analyzed 2 min after the start of the reaction and subsequently every 62.5 min using an on-line GC–MS analyzer (Agilent 7890A with a flame ionization detector and Agilent 5975C mass spectrometer) by using two Restek Rtx-DHA-150 columns. H_2 (Praxair, purity 6.0) was used as the carrier gas.

High-pressure reactions were carried out in a Microactivity Effi setup (PID & Tech), provided with a Sillcoloy-coated stainless steel packed bed reactor with an inner diameter of 8 mm. The temperature was controlled using a K-type

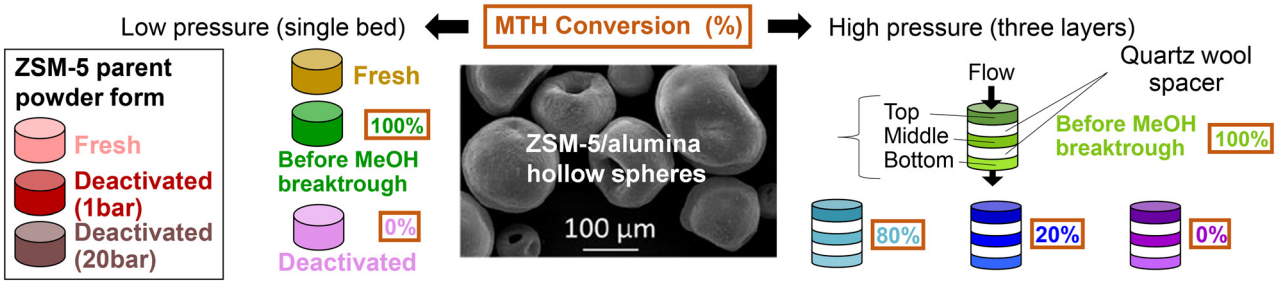

Fig. 1 Description of the 18 samples characterized in this study and the color code used across the document. ZSM-5 parent powder samples are labeled "CBV_" followed by Fresh, or the total pressure for the full deactivated samples, while the spray dried sphere samples are "Sph_" followed by the methanol conversion and the reactor layer: top, middle or bottom. The SEM image in the center was adapted from Fig. 2 of ref. 21.

Open Access Article. Published on 20 november 2025. Downloaded on 17.5.2026. 12.51.47.
This article is licensed under a Creative Commons Attribution 3.0 Unported Licence.

thermocouple inside the catalytic bed. MeOH was fed as a liquid through a Coriolis mass flow controller (mini CORI-FLOW, Bronkhorst) from a pressurized vessel at 20 bar, which was diluted with inert N_2. MeOH and N_2 were premixed in a hot box at 160 °C and flows were stabilized in a bypass mode. Once stable, the preheated mixture was sent to the reactor.

In a typical reaction, three layers of catalysts of about 70 mg separated by quartz wool (Fig. 1, total catalyst weight, *ca.* 210 mg) were placed in the isothermal zone of the reactor. To reach a suitable bed height, inert glass balls and quartz wool were used. Prior to the reaction, the catalyst was activated at 550 °C with a temperature ramp of 10 °C min^{-1} and then isothermally for 1 h under 20% O_2 in N_2. The reactions were carried out under the following conditions to obtain reasonable comparisons with the low-pressure setup: 400 °C, 20 bar total pressure (1.5 bar partial pressure of methanol) and 12.5 $g_{MeOH}\ g_{catalyst}^{-1}\ h^{-1}$ space velocity based on zeolite mass only. The reaction products were analyzed online with a Scion 456 gas chromatograph (GC) equipped with one TCD, two FIDs and six columns (MolSieve 13X, HayeSep Q, HayeSep N, Rt-Stabilwax, Rt-Alumina/MAPD, and Rtx-1). From the reaction products, MTH conversion was defined as the amount of MeOH + dimethyl ether (DME) converted in C basis. Reaction index definitions can be found in the SI (Table S1).

Basic catalyst characterization

The adsorption properties of the materials were evaluated by N_2 adsorption–desorption measurements performed at the N_2 boiling point (−196 °C) on a Bel Belsorp-mini II instrument. Before the measurements, the samples were pretreated under vacuum for 1 h at 80 °C and then for 3 h more at 300 °C. Specific surface area values were calculated using the BET equation. Micropore and mesopore volumes were estimated using the *t*-plot and BJH methods, respectively. The particle size was investigated by scanning electron microscopy (SEM) on a Hitachi SU 8230 FE-SEM instrument with a field emission gun operated at 1 kV. The fresh zeolite samples were fixed on aluminum stubs with double-sided carbon tape. For structural analysis, fresh and deactivated catalysts were analyzed by XRD using a Bruker D8-A25 in a transmission capillary geometry with a Ge (111) Johanssen monochromator and a Lynxeye detector with Cu K-alpha-1 radiation (λ = 1.5406). The samples were placed in 0.7 mm open glass capillaries and the XRD patterns of the hydrated catalysts were measured first. Then, water was removed by heating at 300 °C for 3 h and the capillaries were flame sealed. The X-ray diffractograms of the dried samples were also recorded at 25 °C. The amount of coke species in the catalysts was quantified by thermogravimetric analysis (TGA) on a Netzsch STA 449 TG. Approximately 18 mg of catalyst was heated under 25 mL min^{-1} synthetic air to 800 °C at a rate of 10 °C min^{-1}. Total mass loss is assigned to coke burning plus water removal. The total amount of coke is given in wt% relative to the dried catalyst (mass at 300 °C in the TGA profiles). To calculate the combustion temperatures, the position of the maximum to the 1st derivative of the TGA profiles was fitted to Lorentzian functions.

Absorption tomography

A multiscale tomography system (Skyscan 2211, Bruker, Kontich, Belgium) was used, with an X-ray source operating at 40 kV and a current of 340 μA. The system makes use of a high-resolution CCD camera with a selected field of view spanning 4032 × 2688 pixels, which by setting the distance between the sample and the source, we could reach a final pixel size of 300 nm. For image acquisition, the sample underwent precise stepped rotation over a complete 360 degree scan, with a rotation step of 0.29 degrees. The exposure time was set to 1300 ms and three frames were averaged to ensure a better signal-to-noise ratio. Subsequently, the reconstruction of tomograms from the acquired projection images was executed using the filtered backprojection algorithm provided by the scanner manufacturer.

Powder X-ray diffraction computed tomography

PXRD-CT data were collected at beamline ID15A of the European Synchrotron (ESRF), with a wavelength of 0.18786 Å (determined using NIST SRM 674b CeO_2 during calibration of the 2D detector). The samples were mounted on a Kapton capillary with Araldite to a detector distance of 752 mm. The beam was focused with KB mirrors. An initial low-resolution scan of the whole object was collected to locate the wall of the catalyst spheres with a step size of 50 microns. The final scan was then carried out with a step size of 0.5 microns and 1.8 degree rotations, giving a 298 × 298 voxel region of interest (ROI) for all three samples. The individual exposure time was 0.0485 seconds, which resulted in a total of 72.5 min for each data set. Reconstruction by the filtered back projection method was carried out with in-house Matlab scripts. Data analysis by the Rietveld method was carried out in TOPAS V6 using a sequential refinement approach to refine each tomographic pixel of the slice. The model for the coked ZSM-5 structure was taken from our previous work[11,19,20] and includes dummy atom sites corresponding to the highest electron density peaks in difference Fourier maps of coked ZSM-5 samples. The data were rebinned in TOPAS with a slightly larger step size of 0.02° (from a starting step size of 0.0092°) to reduce the size of the surface least squares calculations. The 2θ range fitted was 0.65 to 9°. The same model was used for all refinements: 16 parameters; 2 for background, lattice parameters and scale factors for gamma alumina and ZSM-5; Lorentzian size broadening for gamma alumina and occupancy of dummy carbon atoms were refined for each individual powder pattern. Finally, isotropic thermal parameters for Si and O of ZSM-5 were fixed to 2 beq and zero error to a refined value of an arbitrary voxel. Non-framework species mass (NFSM), (*a*–*b*) and unit cell volume (UCV) parameters were calculated in the input file for each powder pattern according to our previous definitions.[20] The used

This journal is © The Royal Society of Chemistry 2026

Open Access Article. Published on 20 novembar 2025. Downloaded on 17.5.2026. 12.51.47.
This article is licensed under a Creative Commons Attribution 3.0 Unported Licence.

equation for the computation of XRD descriptors can be found in the SI (Table S1). The whole (ROI) of the reconstructed slice was included in the sequential refinement script and the outlier results coming from empty space were removed by ordering the refinement result matrix in ascending data arrays selecting reasonable ranges of R_{wp}.

Results and discussion

The spray dried catalysts were prepared as described in our previous work.[21] The bulk of the sample presents significant homogeneity in terms of morphology and size distribution (see the optical microscopy images, Fig. S1). Careful examination of the absorption computed tomography (CT) scans, a representative specimen shown in Fig. 2, identifies the real morphology of the catalyst as hollow quasi-spheres of *ca.* 250 microns in size (outer diameter). A three-dimensional model of the object can be rendered by combining all the tomographic slices (Fig. 2A); when sliced, this model also includes the textural properties of the catalyst (Fig. 2B). The advantages of using CT are the fast data collection and the assessment of the heterogeneities such as zeolite crystallites or alumina aggregates, slightly darker due to the difference in electron density of the material and empty spaces. See the reconstructed vertical slice in Fig. 2C; three perpendicular horizontal planes marked as yellow lines are represented in Fig. 2D–F, showcasing the spray drying aperture and a big air bubble across its walls. The wall thickness of the hollow spheres ranged between 15 and 40 microns and contains approximately 35% of active component (ZSM-5) mixed with γ-Al_2O_3 (according to Rietveld refinements, Fig. S2B).

The N_2 adsorption–desorption isotherms of the spheres compared to the parent ZSM-5 polycrystalline sample (Fig. S3) evidenced the huge increase in mesoporosity and a decrease in the micropore volume, which resulted in a significant loss of total specific surface area (Table 1).

Catalytic reactions were performed at two different pressures: 1 and 20 bar. The influence of the total and partial pressure of methanol (see experimental details) on the conversion is shown as a function of reaction time on stream (TOS) in Fig. 3. First, comparing the conversion evolution at ambient pressure (Fig. 3A), the shaped catalyst displayed an almost doubled lifetime compared to the parent material in the powder form. In the first 25 h of the reaction when conversion is still 100%, the selectivity to BTX in the gas phase is 7% in the parent ZSM-5 *versus* 10% in the hollow spheres; C_3 selectivities are 21% and 19%, respectively. Such a tendency in selectivities and the superior lifetime go hand in hand. This has been previously observed and explained on the basis of the better dispersion of ZSM-5 crystals over the inert matrix and the inclusion of mesopores in the materials, which favor the diffusion out of the crystals of the hydrocarbon precursors of coke.[23] Overall, however, the product distribution does not change dramatically, as one would expect from a suitable technical catalyst (Fig. 3B). Nonetheless, this feature is worth mentioning as significant changes in product distribution during MTH have been reported depending on the composition of the catalyst technical body.[13,14,16]

The increase in the total pressure and methanol partial pressure (from 0.3 to 1.5 bar) clearly accelerates deactivation reaching the marked point of 80% conversion after only 40 h

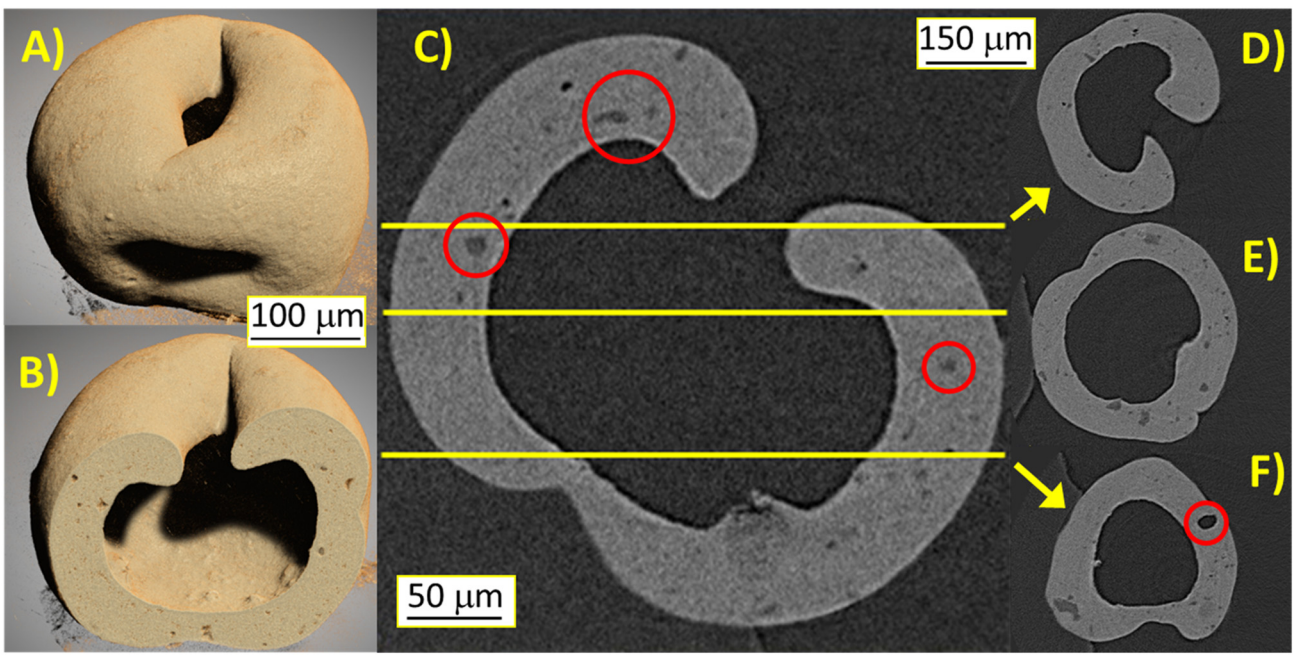

Fig. 2 A) 3D model of absorption computed tomography of the sphere. B) 3D model of the sphere halved for clarity. C) Reconstructed slice of the vertical projection at the center. D)–F) Representative perpendicular reconstructed slices marked in C) as yellow lines.

Open Access Article. Published on 20 novembar 2025. Downloaded on 17.5.2026. 12.51.47.
This article is licensed under a Creative Commons Attribution 3.0 Unported Licence.

Table 1 Full characterization of the samples tested in this work

Conversion (C%)	Coke (dry wt%)	Combustion temperature (°C)	BET area (m^2 g^{-1})	Micropore volume (cm^3 g^{-1})	Mesopore volume (cm^3 g^{-1})
Sph_Fresh	—	—	**329**	**0.06**	**0.30**
CBV_Fresh	—	—	453	0.12	0.08
		1 bar			
Sph_0_1	13.9	566	138	0.01	0.22
Sph_100_1	**6.6**	**546**	**252**	**0.04**	**0.29**
CBV_0_1	13.8	580	131	0.04	0.05
		20 bar			
Sph_0_top	17.4	568	117	0.00	0.20
Sph_0_mid	17.3	559	121	0.00	0.20
Sph_0_bot	14.8	553	152	0.01	0.22
Sph_20_top	**17.9**	**568**	**119**	**0.00**	**0.19**
Sph_20_mid	15.7	562	132	0.01	0.20
Sph_20_bot	13.2	554	190	0.01	0.27
Sph_80_top	14.7	561	148	0.01	0.23
Sph_80_mid	13.7	559	164	0.02	0.22
Sph_80_bot	12.5	557	176	0.02	0.23
Sph_100_top	9.9	552	177	0.01	0.26
Sph_100_mid	6.0	535	252	0.03	0.30
Sph_100_bot	5.6	540	264	0.04	0.30
CBV_0_20	15.8	574	—	—	—

on stream in contrast to 110 h needed at 1 bar (Fig. 3A). Furthermore, the slight increase in aromatic selectivity at full conversion (and paraffins in parallel, Fig. 3B) is likely due to the higher methanol partial pressure, which thermodynamically will favor condensation into heavier products.[24]

A total of 16 fully and partially deactivated samples were produced for *ex situ* characterization by stopping the reaction at different conversion levels (C%, colored symbols in Fig. 3), in addition to the two fresh materials: CBV_Fresh and Sph_Fresh (pure zeolite and spheres with an alumina matrix, respectively). Three deactivated samples were collected at low reaction pressure (1 bar, Sph_(C%)_1 & CBV_0_1). At high-pressure (20 bar), 13 samples were collected, corresponding to different levels of deactivation and different positions in the reactor (catalyst layer, Sph_(C%)_pos) and fully deactivated pure zeolite (CBV_0_20). There is a considerable build-up of hydrocarbon residues measured by TGA (Table 1) well before methanol breakthrough occurs. The amount of total coke increased rapidly before the C2–4 paraffin *versus* olefin ratio, in other words the hydrogen transfer reaction rate significantly decreased, implying again that the aromatic cycle is accelerated at lower TOS values. As the reaction progresses, less aromatic and paraffins were observed until full deactivation was reached, see Fig. S4. These samples were first characterized by N_2 adsorption–desorption (Fig. S5) and TGA (Fig. S6). Table 1 summarizes the main results.

For the fully deactivated pure zeolite (CBV_0_pressure), a slightly higher total amount of coke at high reaction pressure is observed, which one might reasonably expect.[25] However, it is noteworthy that the total amount of coke determined by TGA for the spheres deactivated at low pressure (Sph_0_1) is roughly the same as that for the deactivated pure zeolite (CBV_0_1), 13.9 *vs.* 13.8 wt%, respectively. Considering that only 35 wt% of the spheres are ZMS-5 crystallites, this implies a very significant degree of coke deposition also in the alumina. The situation at 20 bar is even more pronounced (>17 *vs.* 15.8 wt% total coke). It thus seems very likely that coke and/or precursors are formed inside the micropores of the zeolite first, whereafter they migrate to the external part of crystallites and finally when allowed, to the alumina matrix. In a simple view, the alumina acts as a reservoir for the coke, allowing the zeolite component to remain active for an extended period.

For the samples collected at different positions in the catalyst bed, we consistently observe a greater coke deposition in the topmost layers. This agrees well with previous reports,[9,26] and this can be attributed to the "burning cigar" model.[27–29] It has been demonstrated that for zeolite ZSM-5, the MTH reaction and therefore also the coking start near the inlet of the catalyst bed, where a reaction zone is formed, which subsequently gradually moves towards the outlet.[10]

The combustion temperatures calculated from TGA also evolve with the coking levels; the greater the coke content, the higher the combustion temperature. This indicates that the coke matures and evolves into more refractory compounds during extended reaction times, as well documented in the literature.[30] It is interesting to note that the combustion temperature is always higher for the pure zeolites without a binder (Fig. S7), even when compared with the most severely deactivated spheres. This strongly suggests that the external coke also matures further to refractory species when alumina is not present at the vicinity. And that the species accumulated in the mesoporous matrix can be eliminated at lower temperatures.[31,32]

Naturally as more coke is present, less BET surface area is available. Indeed, these metrics are strongly correlated,

 This journal is © The Royal Society of Chemistry 2026

Open Access Article. Published on 20 novembar 2025. Downloaded on 17.5.2026. 12.51.47.
This article is licensed under a Creative Commons Attribution 3.0 Unported Licence.

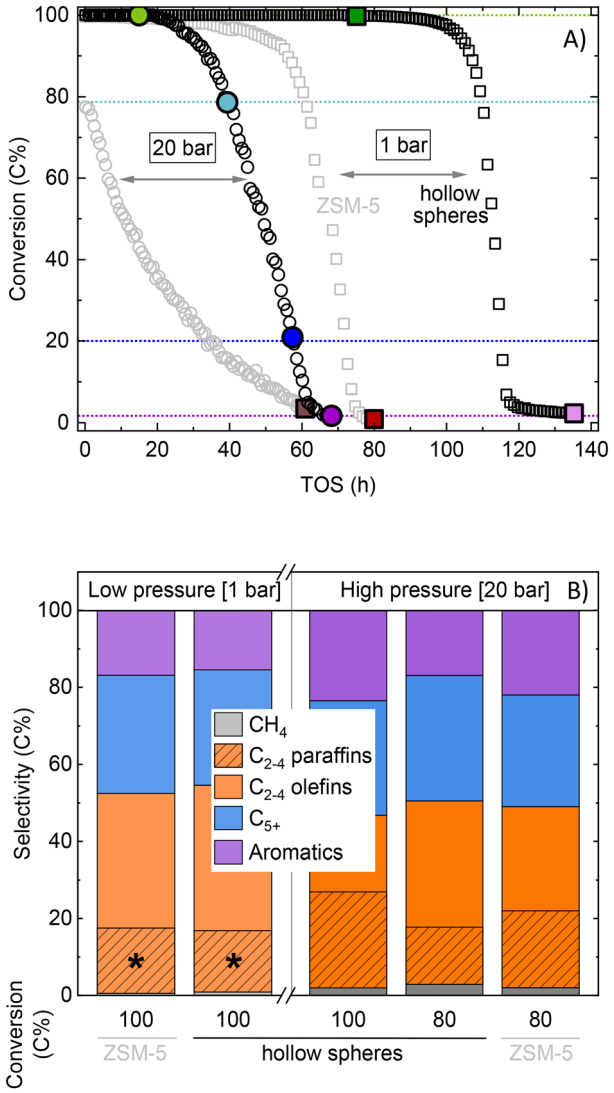

Fig. 3 A) Conversion *versus* TOS curves of the polycrystalline ZSM-5 parent material (grey squares, 1 bar and grey circles, 20 bar) and hollow spheres at low pressure (1 bar, black squares) and high pressure (20 bar, black circles). B) Selectivities in the gas phase at earlier stages of the reaction where hollow sphere samples were analyzed in the solid state. Pressure is specified at the top of the graph. Catalytic activity and samples are defined at the bottom of the bars and the assignment of the selectivities is found in the legend (TOS from left to right are as follows: 1 h, 75 h, 15 h, 40 h and 1 h). (*) The GC–MS connected to the low-pressure reactor (left part of panel B) is not able to separate C_2 paraffins from olefins and the C_3 fraction is convoluted, therefore the quantification in the plot is an estimation assuming a similar C_2 paraffin to olefin ratio to C_3 and C_4.

following a nearly linear trend (Fig. S8A). It is perhaps somewhat surprising that the low- and high-pressure data fit so well in the same plot, including the zeolite without the alumina matrix at low pressure. This again suggests that the coking is relatively uniformly distributed between zeolite and alumina. Further, this allows us to conclude that, in the studied range, the deactivation mechanism is not a function of the total pressure and only the deactivation kinetics are faster because of the higher partial pressure of methanol.

An important part of coke characterization of our study comes from post-mortem XRD analysis of the samples. The correlation between XRD descriptors and deactivation levels has been previously reported for several zeolites.[7,8] Suitable XRD descriptors to interpret the spatially resolved PXRD-CT tomograms are needed.[20] Here, we aim at using the same metrics to evaluate the deactivation state of a more complex system (*i.e.* shaped object) over a diverse range of deactivation levels (see Fig. S9 where raw XRD patterns are shown and S10 for Rietveld refinement examples). We discuss the sensitivity of each descriptor towards ambient moisture (Fig. 4) since it was not possible to control the water content during PXRD-CT data collection. Zeolites are hydrophilic and will adsorb water from the air. All the samples, exposed to months of atmospheric moisture, were loaded in borosilicate capillaries and an initial diffractogram was collected. Then, the capillaries were annealed for water removal and flame sealed. Three XRD based descriptors are analyzed: the difference in the lengths of *a*- and *b*-vectors of the unit cell (referred to as (*a*–*b*)), the unit cell volume (UCV), and the total non-framework species mass (NFSM) as determined from the dummy atom approach. Numerical values are shown in Tables S2 and S3 for dry and moist XRD measurements, respectively. When each XRD descriptor fitted overlaps at the parity lines (represented as diagonal straight lines in Fig. 4), in other words, it yields the same values in both experiments (wet and dry), this means that the descriptor is insensitive to water content. We have previously argued that these descriptors depend on the state of the sample and that they convey slightly different information.[20] The amount of water present and understanding how it affects our XRD descriptors are very relevant in this study because the PXRD-CT experiment could not be accomplished under dry conditions. The (*a*–*b*) descriptor is affected by an anisotropic lattice distortion when the channels of ZSM-5 are filled with aromatic species,[33] but it is unaffected by water content at any degree of deactivation (Fig. 4A). This contrasts with the other two descriptors that present observable deviations from the parity line (Fig. 4B and C, respectively). The total non-framework species mass (NFSM) and the unit cell volume (UCV), in contrast, can be influenced by all kinds of guest species, including volatile compounds and water. The (NFSM) data lie above the parity line, as this metric captures also the water content. The highly coked samples present lower surface area and the Brønsted acid sites (BASs) are blocked, hence it is only natural that less water can be adsorbed (Fig. 4B), and thus the dry and moist descriptors almost converge at high coke content. The presence of water in low coked samples decreases the unit cell volume while the opposite is observed when BASs are blocked by coke (Fig. 4C), in agreement with what was observed in our dehydration experiment of a fully coked crushed cylindrical extrudate.[20]

Two coking mechanisms during the MTH reaction, influenced by the channel size, were differentiated.[34] One in the case of small-window zeotypes (as SAPO-34), where methylated aromatic intermediates cannot diffuse out of the crystals and block the cavities. And the other in bigger-pore

Open Access Article. Published on 20 novembar 2025. Downloaded on 17.5.2026. 12.51.47.
This article is licensed under a Creative Commons Attribution 3.0 Unported Licence.

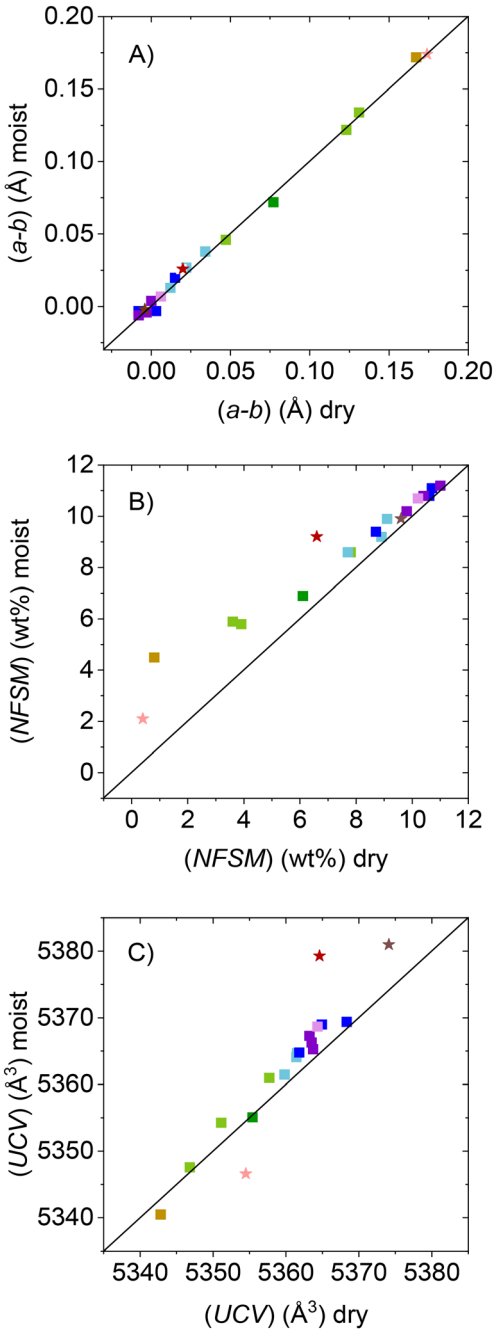

Fig. 4 Parity plots of XRD descriptors for samples equilibrated with moisture *versus* dried samples; A) (*a*–*b*), B) (NFSM) and C) (UCV). The color code used across the whole document is as follows: ochre ■ fresh hollow sphere (Sph_Fresh), green ■, ■ before methanol breakthrough at atmospheric (Sph_100_1) and high-pressure (Sph_100_pos), respectively, blue ■, ■ partially coked at high-pressure at 80% and 20% conversion, respectively, pink ■ fully deactivated at atmospheric pressure (Sph_0_1) and violet ■ fully coked at 20 bar (Sph_0_pos). The red and brown stars correspond to fully coked parent ZSM-5 at 1 (CBV_0_1) and 20 bar (CBV_0_20), respectively, while the flesh star is fresh zeolite (CBV_Fresh).

zeolites (as ZSM-5), where intermediate methylated-benzenes diffuse out, and deactivation is caused by an overloading of these intermediates that condense into bigger coke structures. Based on these mechanisms, we work under the assumption that the presence of the mesopores of the matrix favors the diffusion of these methylated-intermediates out of the crystals. And the more dispersed the zeolite crystals are, the better the mitigation of deactivation is. Therefore, in the case of the pelletized zeolite parent material, methylated intermediates diffuse within the zeolite crystal aggregates and the precursors evolve into larger molecules that block the channels faster. This faster blockage likely occurs partly on the external surface, leaving more empty spaces inside the channels of the zeolites in the parent material as suggested by the larger (NFSM) values that measure only coke in the micropores, of the fully coked spheres (Sph_0_1) compared to pure ZSM-5 zeolite (CBV_0_1), 10.2 *vs.* 6.7 wt%, respectively, and 11 *vs.* 9.5 wt% at 20 bar, respectively (see Table S2, Sph_0_top and CBV_0_20). The discrepancy between the (NFSM) and experimental data measured by TGA suggests an overaccumulation of coke in the external surface of the crystallites and the alumina matrix, which are roughly linearly correlated (Fig. S8B). In this regard, although it is unlikely due to the nature of the MTH reaction and the use of "low temperature" (400 °C) to avoid the thermal formation of coke, we cannot completely discard the direct deposition of some coke in the external surface of the zeolite or the mesoporous matrix, as reported in different processes.[35] In that direction, a possible trend in the lattice parameter of γ-alumina with coking was investigated; however, the results of all the XRD capillary measurements were inconclusive (see Fig. S11A) most likely due to the poor crystallinity of our alumina phase which resulted in severely broad reflections.

One might be tempted to interpret these results, considering the limitations of the analysis, as having a physical limit of internal coke (*i.e.* when the zeolite 10-ring channels are filled with organic molecules) of ~11 wt%. Typically, ZSM-5 holds *ca.* 10–13 wt% TPA+ template after synthesis. Previous work on the same commercial zeolite (CBV 8014), where the adsorption of aromatic species was investigated, showed that a maximum loading in the micropores was achieved in the case of naphthalene (<9 wt%, quantified both by TGA and XRD, (NFSM)).[33] The much higher total coke in the high-pressure experiments (>17 wt%) suggests that the total pressure increases the extent to which coke precursors escape the zeolite channels building up more external coke in the alumina, further supporting the idea that at higher pressure the micropores can be filled to a higher degree. However, the pressure has a somewhat larger effect on the pore filling (NFSM) when the alumina is not present (compare CBV_0_1 and CBV_0_20). For the fully coked spheres at low pressure (Sph_0_1), the pore filling (NFSM) is already very close to the theoretical maximum internal coke, 11 wt%. More accessibility for coke precursors to escape also means more accessibility for methanol to enter the micropore volume before it becomes completely blocked.

In view of the different sensitivities of the three XRD descriptors towards moisture and considering that it was not possible to control moisture during the PXRD-CT

 This journal is © The Royal Society of Chemistry 2026

Open Access Article. Published on 20 november 2025. Downloaded on 17.5.2026. 12.51.47.
This article is licensed under a Creative Commons Attribution 3.0 Unported Licence.

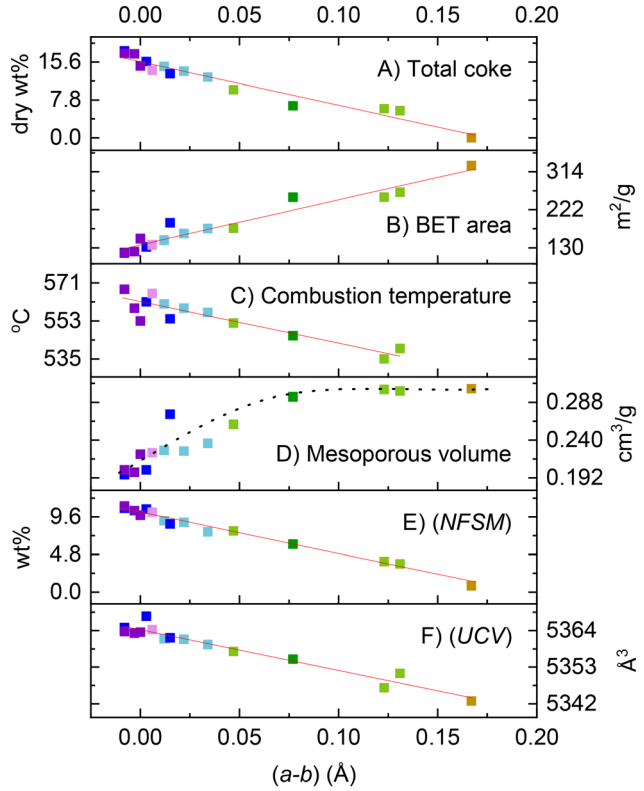

Fig. 5 Correlations of the (*a*–*b*) descriptor with: A) total coke (dry wt%), B) BET surface area, C) combustion temperature of coke, D) mesopore volume, E) non framework species mass (wt%) from the dry data set and F) unit cell volume.

experiments, we focused on the (*a*–*b*) descriptor to extract physically meaningful information for our material (Fig. 5). Some physicochemical properties of the used materials follow a nice linear trend with the descriptor. A linear fitting with an R^2 of 0.93 is obtained for the properties measured in Fig. S4 to describe deactivation, *i.e.*, total coke content (Fig. 5A) and specific surface area (Fig. 5B). From the first derivative of TGA profiles, the combustion temperature of the deposited coke can be extracted (Fig. S6). The combustion temperature of coke has been used for hypothesizing on the location (external *vs.* internal coke) and nature of coke (aliphatic *vs.* refractory), with refractory species inside the zeolite crystals being the most difficult to burn off.[23] The relationship of this temperature to our (*a*–*b*) descriptor, together with the mesopore evolution (characteristic of the matrix in the hollow spheres, isotherms in Fig. S5), allows us to elucidate how the coke species evolve and affect the shaped catalyst (Fig. 5C and D). The linear trend of the coke combustion temperature with the (*a*–*b*) descriptor suggests a natural increase in the coke inside the zeolite crystals of a more refractory and inert nature as deactivation occurs, which distorts the framework of the zeolite. Otherwise, no significant decay in the mesoporous volume is noticeable before conversion starts to drop (see the significant parallel drop in the BET surface area and combustion temperature). Then, the mesopore volume (which is associated largely with the binder) decreases faster when the zeolite framework is significantly distorted (Fig. 5D).

These results again suggest the hypothesis of an initial filling of the zeolite crystals with HCP species, which gradually mature to coke-like species that distort the lattice upon a concentration increase while still being able to diffuse out to the catalyst matrix and perhaps keep evolving there. This hypothesis is in good agreement with the "overloading" deactivation mechanism reported by Qi *et al.*[36] for HZSM-5 during MTH. According to these authors, the main cause of HZSM-5 deactivation, especially at low temperature and high density of BASs, may well be the accumulation of HCP species inside the channels and not necessarily the formation of hard coke that blocks the pores externally. They proposed an improvement of catalyst diffusivity to alleviate deactivation, which is in line with the increase in the lifetime we have observed for the hollow spheres. Please see the perfect fitting (R^2 of 0.98) of the (NFSM) dry and (*a*–*b*) descriptors in Fig. 5E which reinforces the idea that both are sensitive to internal coke in the absence of water. Lastly, a more scattered trend is observed for the two descriptors deduced from lattice parameters or with (NFSM) when accounting samples with moisture, Fig. S11B. Nonetheless, and even though we cannot directly correlate the computed values to physical properties experimentally, additional spatially resolved information can be extracted from the PXRD-CT analysis.

Recent structural chemistry studies typically used 1 mm beam size, for example to study heterogeneities within a battery electrode upon electrochemical cycling[37–39] or the degradation of a multicomponent FCC catalyst.[40] Although state-of-the-art nanofocused collimation at synchrotron facilities can provide beam sizes in the range of 0.15–0.5 mm,[22] this work lies at the forefront in the field of catalyst PXRD-CT. The data collection strategy allowed slices of a refinable matrix at 0.125 μm^3 per voxel resolution (see Fig. S12 for data quality assessment of single voxels) which represents, to the best of our knowledge, the highest resolution ever reported on a similar study. This is perhaps due to the limited quality of reconstructed diffractograms for each of these small voxels at such a resolution and the longer data collection strategy, impractical for *in situ* and/or operando studies and investigations of larger objects. Three selected samples were analyzed to compare the evolution in detail of the coking during deactivation: Sph_Fresh, Sph_100_1 and Sph_20_top. The big advantage of PXRD-CT over absorption CT is the possibility of studying the crystalline phase distribution in shaped objects,[17] not easily investigated otherwise. Brief examination of Fig. 6 reveals that the object walls contain 1–2 μm large zeolite crystallites spread out individually and/or forming agglomerates. This is in agreement with the crystal morphology and particle size of the parent material assessed by SEM (Fig. S13). In the case of the alumina, although some big aggregates were observed in the absorption CT scans (Fig. 2), they seem to be generally more homogeneously distributed within the bulk of the catalyst walls.

In addition to phase distribution analysis, exploring how crystal structure parameters are spatially resolved is the true

Open Access Article. Published on 20 november 2025. Downloaded on 17.5.2026. 12.51.47.
This article is licensed under a Creative Commons Attribution 3.0 Unported Licence.

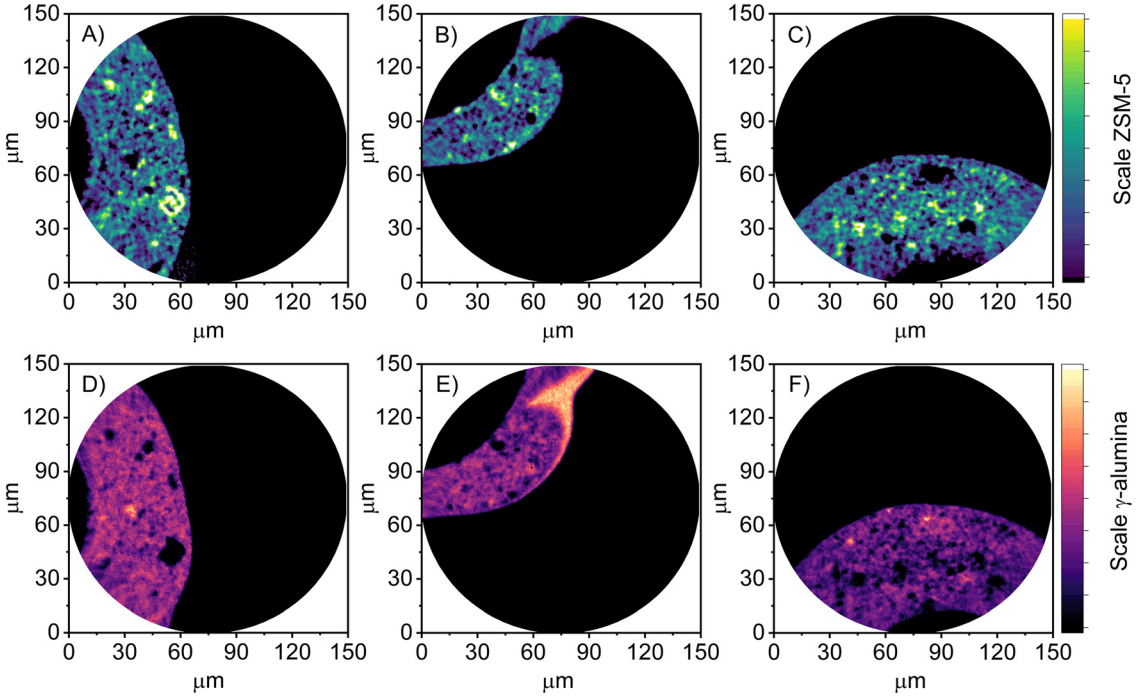

Fig. 6 PXRD-CT reconstructed slices of the three (A and D) fresh, (B and E) partially coked and (C and F) fully coked samples, showing the scale factor refined during Rietveld analysis of the two crystallographic phases: zeolite on top and binder on the bottom.

power of PXRD-CT. In this scenario, where water could not be removed from the samples due to experimental limitations, the (*a*–*b*) descriptor (Fig. 7A–C) is the most useful as we demonstrated before (Fig. 4). The presence of water limits the applicability of our dummy atom model (NFSM) that takes any electron density inside the zeolite channels (Fig. 7D–F). Therefore, the (NFSM) values cannot be directly correlated with estimations of the amount of coke in the micropores, although they provide the notion of having some perhaps small organic molecules filling the channels of the zeolite in both 100% conversion and severely deactivated samples, Fig. 7E and F. It comes as no surprise that retrieving information with regard to the (UCV) descriptor (Fig. 7G–I) is very limited due to the small beam and fast data collection used resulting in low resolution diffraction patterns and even further dispersion of the (UCV) values was observed for the moist samples (Fig. 4C). Note that ZSM-5 wt% is also plotted in the figure to give further contrast to the figure, which highlights the zeolite descriptors refined in the locations where a large zeolite fraction is found. A comparison between such a plot and the scale of ZSM-5 can be found in the SI. Note that they look very similar since the results with high residuals were filtered out to exclude air bubbles and empty spaces (Fig. S14). We focused on the results of (*a*–*b*), the best XRD descriptor in this case study, for partially and fully coked samples, represented in Fig. 7B and C. The values of (*a*–*b*) clearly decrease with increasing degree of deactivation, as seen above. However, the whole wall of the object appears to be homogeneous with no coking gradients observed. The main conclusion of our PXRD-CT study is therefore that the entire mass of the catalyst in the spherical bodies is accessible to reactants, meaning that this type of spray dried catalyst body is a promising way to avoid internal diffusion limitations observed in pellet bodies with PXRD-CT and other techniques.[19,20,41,42]

Tables S2–S4 show that the XRD descriptors for different stages of coking from PXRD-CT (weighted by the refined ZSM-5 scale factor mean) and those observed in capillary XRD of bulk samples are relatively comparable. Discrepancies in the comparison of bulk capillary XRD and PXRD-CT results highlight the variability within the reactor.[10] When we consider the well-known "burning cigar" model for ZSM-5, it is only reasonable to assume that not all the spheres are deactivated to exactly the same degree, especially in the case of the partially coked sample.

Conclusions

A hollow sphere catalyst material for the methanol to hydrocarbon (MTH) reaction was prepared by spray drying with a composition of 35 wt% ZSM-5/65 wt% alumina. A significant improvement in the catalyst lifetime was observed for the shaped catalysts. To track deactivation, the MTH reaction was stopped at different stages (*i.e.* conversion levels) and the used samples were characterized by TGA, N_2 adsorption–desorption and capillary XRD to quantify the amount of coke and elucidate its evolution during the reaction. Clearly, there is a pronounced accumulation of coke on the alumina matrix, which is suggested to come from migration of coke (precursors) from the zeolite channels. These results highlight the benefit of having a mesoporous matrix that barely participates in the reaction (selectivities

 This journal is © The Royal Society of Chemistry 2026

Open Access Article. Published on 20 novembar 2025. Downloaded on 17.5.2026. 12.51.47.
This article is licensed under a Creative Commons Attribution 3.0 Unported Licence.

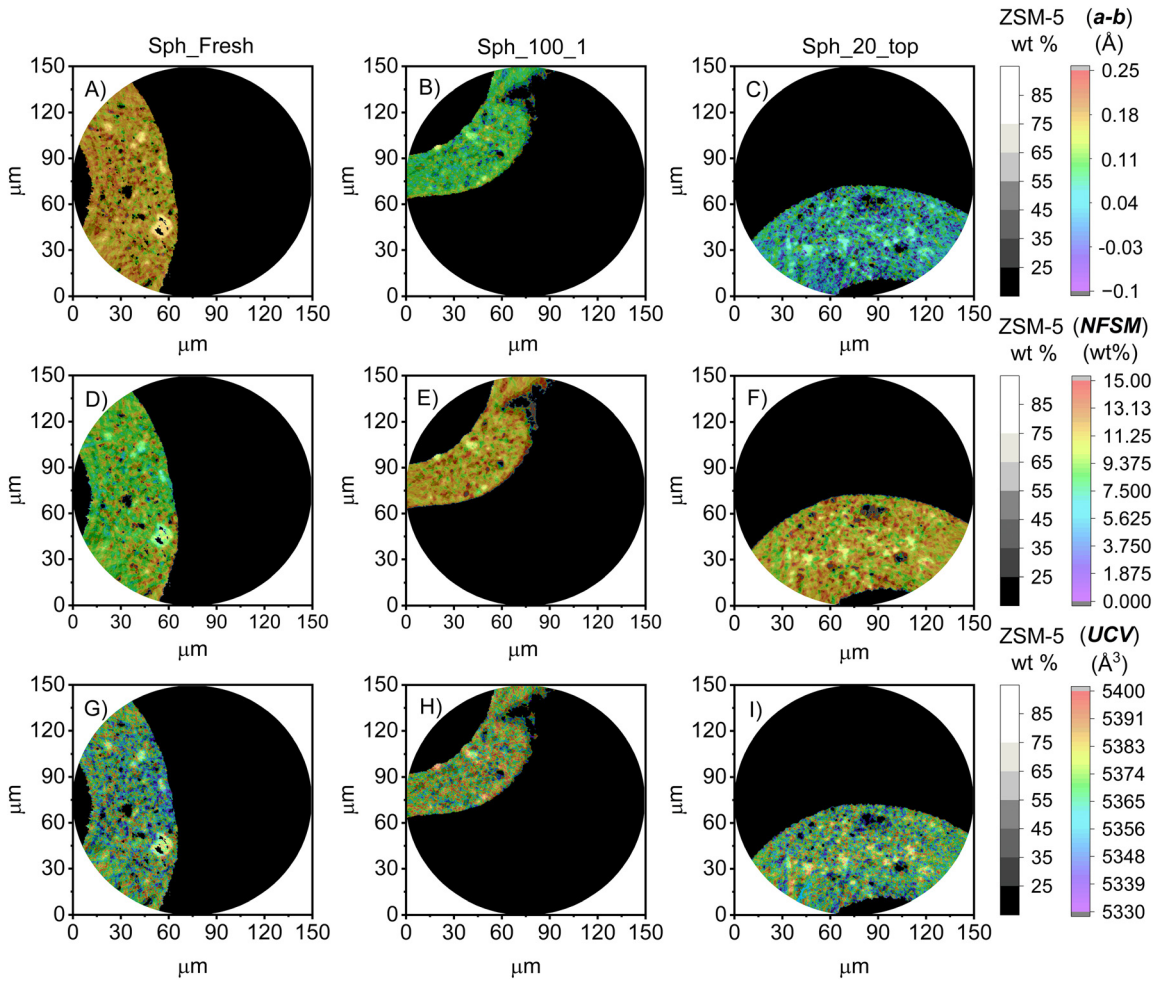

Fig. 7 Reconstructed slices of PXRD-CT refined. Black and white represent the zeolite/alumina refined volume fraction (air is also represented in black for clarity). XRD descriptors: (A–C) on top with (*a*–*b*), (D–F) in the middle with (NFSM) and (G)–I) on the bottom with (UCV), of fresh (left), 100% conversion (middle) and 20% conversion (right) catalysts.

consistent with polycrystalline tests) but significantly enhances the catalyst lifetime. Higher pressure in the reactor resulted in a mild increase in the total coking of the sphere. An improvement in the catalyst lifetime was observed for the shaped object. Our well proven XRD descriptors allowed us to monitor the deactivation by coking. This work pushes the boundaries of PXRD-CT with an extremely high voxel resolution and paves the way towards advancements from powder to shaped catalyst objects. We successfully processed a huge data set (almost a million diffractograms per tomogram in total, high- and low-resolution regions combined) and demonstrated the suitability of the (*a*–*b*) descriptor for *ex situ* experiments at constant temperature, as opposed to (NFSM) or (UCV), for which coking effects are convoluted with those of ambient moisture. By doing so, we were able to demonstrate that these hollow quasi-spherical extrudates do not present coking gradients in the walls, thus overcoming diffusion limitations. Therefore, the accessibility of the spray dried catalytic material is optimized for this composition, as opposed to cylindrical extrudates with similar components studied before.[19] Although the direct use of this catalyst formulation in industrial reactors would require further studies to improve the particle size or mechanical resistance, it offers the possibility of studying optimal compositions of technical catalysts as model systems, avoiding the usual diffusion limitations of lab-scale testing objects.

Author contributions

CRediT authorship contribution statements: Izar Capel Berdiell: conceptualization, methodology, formal analysis, investigation, data curation, writing – original draft, writing – review & editing, visualization. Tomás Cordero-Lanzac: conceptualization, formal analysis, investigation, data curation, writing – original draft, writing – review & editing, visualization. Nicolai H. Junge: formal analysis, investigation, data curation. Liebert P. Nogueira: methodology, formal analysis, investigation, data curation. Gavin Vaughan: formal analysis, investigation, data curation. Marco Di Michiel: methodology, formal analysis, investigation, data curation. Pablo Beato: conceptualization, resources, funding acquisition. Lars F. Lundegaard: conceptualization, methodology,

Open Access Article. Published on 20 november 2025. Downloaded on 17.5.2026. 12.51.47.
This article is licensed under a Creative Commons Attribution 3.0 Unported Licence.

investigation, writing – review & editing, funding acquisition. David S. Wragg: conceptualization, methodology, formal analysis, investigation, resources, data curation, writing – original draft, writing – review & editing, supervision, funding acquisition. Stian Svelle: conceptualization, investigation, resources, writing – original draft, writing – review & editing, supervision, funding acquisition.

Conflicts of interest

There are no conflicts to declare.

Data availability

The data supporting this article have been included as part of the supplementary information (SI).

Supplementary information is available. See DOI: https://doi.org/10.1039/d5cy01023c.

Acknowledgements

The authors acknowledge ESRF for granting beamtime at ID15A (ch-5896 & ih-ch-1624). The Research Council of Norway is acknowledged for the support *via* the TomoCAT researcher project (project no. 301619). We acknowledge the use of the Norwegian national infrastructure for X-ray diffraction and scattering (RECX, RCN project no. 208896). We also acknowledge Irene Pinilla-Herrero for the manufacturing of the spheres.

References

1 C. Mei, P. Wen, Z. Liu, H. Liu, Y. Wang, W. Yang, Z. Xie, W. Hua and Z. Gao, *J. Catal.*, 2008, **258**, 243–249.
2 M. Wen, X. Wang, L. Han, J. Ding, Y. Sun, Y. Liu and Y. Lu, *Microporous Mesoporous Mater.*, 2015, **206**, 8–16.
3 B. C. Bukowski, *Nat. Catal.*, 2023, **6**, 222–223.
4 E. Borodina, H. S. H. Kamaluddin, F. Meirer, M. Mokhtar, A. M. Asiri, S. A. Al-Thabaiti, S. N. Basahel, J. Ruiz-Martinez and B. M. Weckhuysen, *ACS Catal.*, 2017, **7**, 5268–5281.
5 J. Goetze and B. M. Weckhuysen, *Catal. Sci. Technol.*, 2018, **8**, 1632–1644.
6 P. Rzepka, D. Sheptyakov, C. Wang, J. A. van Bokhoven and V. Paunović, *ACS Catal.*, 2024, **14**, 5593–5604.
7 I. Capel Berdiell, G. B. Braghin, T. Cordero-Lanzac, P. Beato, L. F. Lundegaard, D. Wragg, S. Bordiga and S. Svelle, *Top. Catal.*, 2023, **66**, 1418–1426.
8 L. F. Lundegaard, I. C. Berdiell, N. König, N. H. Junge, P. Beato, D. Chernyshov, S. Svelle and D. S. Wragg, *Microporous Mesoporous Mater.*, 2024, **366**, 112911.
9 D. Rojo-Gama, M. Nielsen, D. S. Wragg, M. Dyballa, J. Holzinger, H. Falsig, L. F. Lundegaard, P. Beato, R. Y. Brogaard, K. P. Lillerud, U. Olsbye and S. Svelle, *ACS Catal.*, 2017, **7**, 8235–8246.
10 D. Rojo-Gama, L. Mentel, G. N. Kalantzopoulos, D. K. Pappas, I. Dovgaliuk, U. Olsbye, K. P. Lillerud, P. Beato, L. F. Lundegaard, D. S. Wragg and S. Svelle, *J. Phys. Chem. Lett.*, 2018, **9**, 1324–1328.
11 G. N. Kalantzopoulos, D. Rojo Gama, D. K. Pappas, I. Dovgaliuk, U. Olsbye, P. Beato, L. F. Lundegaard, D. S. Wragg and S. Svelle, *Dalton Trans.*, 2022, **51**, 16845–16851.
12 D. S. Wragg, D. Akporiaye and H. Fjellvåg, *J. Catal.*, 2011, **279**, 397–402.
13 N.-L. Michels, S. Mitchell and J. Pérez-Ramírez, *ACS Catal.*, 2014, **4**, 2409–2417.
14 S. Zhang, Y. Gong, L. Zhang, Y. Liu, T. Dou, J. Xu and F. Deng, *Fuel Process. Technol.*, 2015, **129**, 130–138.
15 T. Shoinkhorova, A. Dikhtiarenko, A. Ramirez, A. Dutta Chowdhury, M. Caglayan, J. Vittenet, A. Bendjeriou-Sedjerari, O. S. Ali, I. Morales-Osorio, W. Xu and J. Gascon, *ACS Appl. Mater. Interfaces*, 2019, **11**, 44133–44143.
16 A. Sanz-Martínez, J. Lasobras, J. Soler, J. Herguido and M. Menéndez, *Catalysts*, 2022, **12**, 134.
17 A. Vamvakeros, S. D. M. Jacques, M. Di Michiel, D. Matras, V. Middelkoop, I. Z. Ismagilov, E. V. Matus, V. V. Kuznetsov, J. Drnec, P. Senecal and A. M. Beale, *Nat. Commun.*, 2018, **9**, 4751.
18 P. Senecal, S. D. M. Jacques, M. Di Michiel, S. A. J. Kimber, A. Vamvakeros, Y. Odarchenko, I. Lezcano-Gonzalez, J. Paterson, E. Ferguson and A. M. Beale, *ACS Catal.*, 2017, **7**, 2284–2293.
19 D. S. Wragg, G. N. Kalantzopoulos, D. K. Pappas, I. Pinilla-Herrero, D. Rojo-Gama, E. Redekop, M. Di Michiel, P. Beato, L. F. Lundegaard and S. Svelle, *J. Catal.*, 2021, **401**, 1–6.
20 I. Capel Berdiell, L. F. Lundegaard, P. Beato, M. Di Michel, D. S. Wragg and S. Svelle, *J. Catal.*, 2025, **450**, 116300.
21 I. Pinilla-Herrero, E. Borfecchia, T. Cordero-Lanzac, U. V. Mentzel, F. Joensen, K. A. Lomachenko, S. Bordiga, U. Olsbye, P. Beato and S. Svelle, *J. Catal.*, 2021, **394**, 416–428.
22 N. E. Omori, A. D. Bobitan, A. Vamvakeros, A. M. Beale and S. D. M. Jacques, *Philos. Trans. R. Soc., A*, 2023, **381**, 20220350.
23 T. Cordero-Lanzac, A. Ateka, P. Pérez-Uriarte, P. Castaño, A. T. Aguayo and J. Bilbao, *Ind. Eng. Chem. Res.*, 2018, **57**, 13689–13702.
24 U. Olsbye, S. Svelle, M. Bjørgen, P. Beato, T. V. W. Janssens, F. Joensen, S. Bordiga and K. P. Lillerud, *Angew. Chem., Int. Ed.*, 2012, **51**, 5810–5831.
25 N. Kosinov, E. A. Uslamin, L. Meng, A. Parastaev, Y. Liu and E. J. M. Hensen, *Angew. Chem., Int. Ed.*, 2019, **58**, 7068–7072.
26 D. Rojo-Gama, S. Etemadi, E. Kirby, K. P. Lillerud, P. Beato, S. Svelle and U. Olsbye, *Faraday Discuss.*, 2017, **197**, 421–446.
27 J. F. Haw and D. M. Marcus, *Top. Catal.*, 2005, **34**, 41–48.
28 H. Schulz, *Catal. Today*, 2010, **154**, 183–194.
29 J. S. Martinez-Espin, M. Mortén, T. V. W. Janssens, S. Svelle, P. Beato and U. Olsbye, *Catal. Sci. Technol.*, 2017, **7**, 2700–2716.
30 M. D. P. Sørensen, *Chem. Eng. Sci.*, 2017, **168**, 465–479.
31 M. Ibáñez, P. Pérez-Uriarte, M. Sánchez-Contador, T. Cordero-Lanzac, A. T. Aguayo, J. Bilbao and P. Castaño, *Catalysis*, 2017, **7**, 254.
32 B. J. B. Silva, L. V. Sousa, L. R. A. Sarmento, A. C. S. Melo, D. S. Silva, P. H. L. Quintela, S. L. Alencar and A. O. S. Silva, *J. Therm. Anal. Calorim.*, 2022, **147**, 3161–3170.

This journal is © The Royal Society of Chemistry 2026

Open Access Article. Published on 20 novembar 2025. Downloaded on 17.5.2026. 12.51.47.
This article is licensed under a Creative Commons Attribution 3.0 Unported Licence.

33 A. Seremak, I. Capel Berdiell, B. Arstad, T. Fjermestad and S. Svelle, *J. Phys. Chem. C*, 2025, **129**, 1183–1197.
34 L. Qi, J. Li, L. Wang, C. Wang, L. Xu and Z. Liu, *Catal. Sci. Technol.*, 2017, **10**, 2022–2031.
35 S. Weber, D. Karpov, M. Kahnt, A. Diaz, Y. Romanenko, S. Kotrel, A. Haas, B. Hinrichsen, N. Bottke, J.-D. Grunwaldt, S. Schunk and T. L. Sheppard, *ChemCatChem*, 2024, **16**, e202301298.
36 L. Qi, J. Li, L. Wang, L. Xu and Z. Liu, *Catal. Sci. Technol.*, 2017, **7**, 894–901.
37 D. P. Finegan, A. Vamvakeros, L. Cao, C. Tan, T. M. M. Heenan, S. R. Daemi, S. D. M. Jacques, A. M. Beale, M. Di Michiel, K. Smith, D. J. L. Brett, P. R. Shearing and C. Ban, *Nano Lett.*, 2019, **19**, 3811–3820.
38 S. R. Daemi, C. Tan, A. Vamvakeros, T. M. M. Heenan, D. P. Finegan, M. Di Michiel, A. M. Beale, J. Cookson, E. Petrucco, J. S. Weaving, S. Jacques, R. Jervis, D. J. L. Brett and P. R. Shearing, *Phys. Chem. Chem. Phys.*, 2020, **22**, 17814–17823.
39 D. P. Finegan, A. Vamvakeros, C. Tan, T. M. M. Heenan, S. R. Daemi, N. Seitzman, M. Di Michiel, S. Jacques, A. M. Beale, D. J. L. Brett, P. R. Shearing and K. Smith, *Nat. Commun.*, 2020, **11**, 631.
40 M. Gambino, M. Veselý, M. Filez, R. Oord, D. Ferreira Sanchez, D. Grolimund, N. Nesterenko, D. Minoux, M. Maquet, F. Meirer and B. M. Weckhuysen, *Angew. Chem., Int. Ed.*, 2020, **59**, 3922–3927.
41 D. Mores, E. Stavitski, M. H. F. Kox, J. Kornatowski, U. Olsbye and B. M. Weckhuysen, *Chem. – Eur. J.*, 2008, **14**, 11320–11327.
42 I. L. C. Buurmans and B. M. Weckhuysen, *Nat. Chem.*, 2012, **4**, 873–886.